

# A Practical Approach to Optimal Estimator Design in RAIM

Mathieu Joerger and Boris Pervan, *Illinois Institute of Technology*

## BIOGRAPHIES

**Dr. Mathieu Joerger** obtained a Master in Mechatronics from the National Institute of Applied Sciences in Strasbourg, France, in 2002, and a M.S. and a Ph.D. in Mechanical and Aerospace Engineering from the Illinois Institute of Technology (IIT), in 2002 and 2009 respectively. He is the 2009 recipient of the Institute of Navigation (ION) Bradford Parkinson award, which honors outstanding graduate students in the field of GNSS. He is currently a research assistant professor at IIT, working on multi-sensor integration, on sequential fault-detection for multi-constellation navigation systems, and on relative and differential receiver autonomous integrity monitoring (RAIM) for shipboard landing of military aircraft.

**Dr. Boris Pervan** is a Professor of Mechanical and Aerospace Engineering at IIT, where he conducts research on advanced navigation systems. Prior to joining the faculty at IIT, he was a spacecraft mission analyst at Hughes Aircraft Company (now Boeing) and a postdoctoral research associate at Stanford University. Prof. Pervan received his B.S. from the University of Notre Dame, M.S. from the California Institute of Technology, and Ph.D. from Stanford University. He is an Associate Fellow of the AIAA, a Fellow of the Institute of Navigation (ION), and Editor-in-Chief of the ION journal NAVIGATION. He was the recipient of the IIT Sigma Xi Excellence in University Research Award (2011, 2002), Ralph Barnett Mechanical and Aerospace Dept. Outstanding Teaching Award (2009, 2002), Mechanical and Aerospace Dept. Excellence in Research Award (2007), University Excellence in Teaching Award (2005), IEEE Aerospace and Electronic Systems Society M. Barry Carlton Award (1999), RTCA William E. Jackson Award (1996), Guggenheim Fellowship (Caltech 1987), and Albert J. Zahm Prize in Aeronautics (Notre Dame 1986).

## ABSTRACT

This paper presents new methods to find the optimal non-least-squares (NLS) estimator that minimizes the integrity risk in Receiver Autonomous Integrity Monitoring (RAIM). These methods aim at lowering the integrity risk in exchange for a slight increase in nominal

positioning error. A first algorithm is formulated as a multi-dimensional minimization problem, which directly minimizes integrity risk, but can only be solved using a time-consuming iterative process involving the integration of a bivariate normal distribution. Then, parity space representations are exploited to develop a new computationally-efficient, near-optimal NLS-estimator design method, which uses a straightforward line-search process. Performance analyses for an example multi-constellation Advanced RAIM (ARAIM) application show that this new method enables significant integrity risk reduction, even in real-time implementations where computational resources are limited.

## I. INTRODUCTION

This paper describes the design, analysis and evaluation of new methods to determine the optimal estimator that minimizes the integrity risk in Receiver autonomous integrity monitoring (RAIM) [1], [2].

RAIM exploits redundant measurements to achieve self-contained fault detection at the user receiver. With the modernization of GPS, the full deployment of GLONASS, and the emergence of Galileo and Beidou, an increased number of redundant ranging signals becomes available, which has recently drawn a renewed interest in RAIM. In particular, RAIM can help alleviate requirements on ground monitors. For example, researchers in the European Union and in the United States are investigating Advanced RAIM (ARAIM) for worldwide vertical guidance of aircraft [3].

One of the primary tasks in RAIM is to evaluate the integrity risk, which is the probability of undetected faults causing unacceptably large errors in the estimated position [4]. Integrity risk evaluation involves both assessing the fault-detection capability and quantifying the impact of undetected faults on position estimation errors. Hence, both the detector and the estimator influence RAIM performance.

The RAIM detector and estimator have both been investigated in the literature. RAIM detectors were analyzed in [5] and [6], which showed that for realistic navigation requirements, the optimal detector, which minimizes the integrity risk, approaches the solution

separation (SS) RAIM detector. Therefore, SS test statistics are used in this work as they provide a computationally-efficient, practical approximation of the optimal detection region.

In parallel, with regard to estimation, researchers have explored the potential of replacing the conventional least-squares (LS) process with a non-least-squares (NLS) estimator to lower the integrity risk in exchange for a slight increase in nominal positioning error [7], [8], [9]. The resulting methods show promising reductions in integrity risk, but are either non-optimal [7], [8] or computationally expensive [9].

In response, this paper provides new methods to determine the optimal estimator in RAIM, which minimizes integrity risk. Of particular concern is the fact that the new estimator design methods may be implemented in applications where processing resources are limited. In this perspective, a computationally-efficient, near-optimal algorithm is developed, and the tradeoff between increasing computation time and decreasing integrity risk is quantified.

Section II of this paper describes the conventional LS estimator-based SS RAIM method (derived in [10] and, e.g., implemented in [11]) using parity space representations. The parity vector is the simplest, most fundamental expression of detection capability [12]. Section II explains, for example, that the SS RAIM detection boundary is a polytope in parity space [13]. This graphical representation is used throughout Sections III and IV to modify the integrity risk evaluation process.

In Section III, new methods are established to design NLS estimators. The first algorithm aims at minimizing integrity risk, subject to a false alarm constraint, regardless of computation load. The method avoids making conservative assumptions used in [9], which are discussed in this paper. Instead, the method resorts to direct integrity risk evaluation (DIRE), thereby providing the means to quantify the highest-achievable integrity performance. In this case, the NLS estimator design process is formulated as a multi-dimensional optimization (MDO) problem, which is solved using a time-consuming iterative procedure.

This ‘DIRE MDO’ serves as a starting point for Section IV, where a second method is developed to reduce processing time while still providing lower integrity risk than conventional LS-based RAIM. Section IV presents a one-dimensional optimization (ODO) process to approximate the MDO, and an integrity risk bounding method (IB) to replace the DIRE. On the one hand, the integrity risk increases slightly due to conservative bounding assumptions detailed in the paper. On the other hand, the considerable simplifications from MDO to

ODO, and from DIRE to IB result in a computationally-efficient ‘IB ODO’ method.

To quantify the drop in processing time from DIRE MDO to IB ODO, a performance analysis is carried out. Worldwide availability maps are established for an example aircraft approach application using Advanced RAIM (ARAIM) with dual-frequency GPS and Galileo satellite measurements. The results show that availability using a NLS estimator is much higher than using the LS estimator, and that the IB ODO NLS-estimator-design method accomplishes an effective compromise between run time and availability performance, as compared to both DIRE and to conventional LS-based RAIM method.

## II. BACKGROUND ON SOLUTION SEPARATION RAIM USING A LEAST-SQUARES ESTIMATOR

### A. General Integrity and Continuity Risk Definitions

The general definition of the integrity risk, or probability of hazardous misleading information (HMI), is given by:

$$P_{HMI} \equiv P(|\varepsilon| > \ell, |q| < T) \quad (1)$$

where

|               |  |
|---------------|--|
| $\varepsilon$ | is the error on the estimated parameter of interest (called ‘state’ of interest)                                       |
| $\ell$        | is a specified alert limit that defines hazardous situations (e.g., specified in [4] for aircraft approach navigation) |
| $q$           | is the detection test statistic  |
| $T$           | is the detection threshold   |

Considering a set of  $h+1$  mutually exclusive, jointly exhaustive hypotheses  $H_i$ , the law of total probability can be used to express the integrity criterion as:

$$P_{HMI} = \sum_{i=0}^h P(|\varepsilon| > \ell, |q| < T \mid H_i) P_{Hi} \leq I_{REQ} \quad (2)$$

where:

|           |  |
|-----------|--|
| $I_{REQ}$ | is the integrity risk requirement (also specified in [4] for example aviation applications).   |
| $P_{Hi}$  | is the prior probability of $H_i$ occurrence   |
| $H_0$     | is the fault-free hypothesis   |
| $H_i$     | for $i=1, \dots, h$ are the fault hypotheses corresponding to faults on subset measurement ‘ $i$ ’ (including single-satellite and multi-satellite faults) |

References [13] and [14] give procedures to limit the number of fault hypotheses that need to be monitored

against, while still accounting for all other fault hypotheses in the overall integrity risk evaluation.

Under fault-free hypothesis  $H_0$ , the detection threshold  $T$  is typically set based on an allocated continuity risk requirement  $C_{REQ}$  (e.g., specified in [4]) to limit the probability of false alarms.  $T$  can be defined as:

$$P(|q| \geq T \mid H_0) \leq C_{REQ} \quad (3)$$

### B. Measurement Equation and Least-Squares Estimator

The joint probability in equation (2) is a function of two random variables  $\varepsilon$  and  $q$ , both derived from a measurement equation. Let  $n$  and  $m$  respectively be the number of measurements and number of states, and let  $\mathbf{z}_*$  be the  $n \times 1$  vector of stacked measurements. This work assumes that the cumulative distribution function (CDF) of nominal measurement errors is bounded by a zero mean Gaussian distribution with covariance matrix  $\mathbf{V}_*$  [15]. Vector  $\mathbf{z}_*$  is pre-multiplied by  $\mathbf{V}_*^{-1/2}$  to obtain the ‘normalized’ measurement equation:

$$\mathbf{z} = \mathbf{H}\mathbf{x} + \mathbf{v} + \mathbf{f} \quad (4)$$

where

$\mathbf{z} = \mathbf{V}_*^{-1/2} \mathbf{z}_*$  is  $n \times 1$  the normalized measurement vector  
 $\mathbf{H}$  is the  $n \times m$  normalized observation matrix,  
 $\mathbf{x}$  is the  $m \times 1$  state vector,  
 $\mathbf{f}$  is the  $n \times 1$  normalized fault vector.  
 $\mathbf{v}$  is the  $n \times 1$  normalized measurement noise vector composed of zero-mean, unit-variance independent and identically distributed (i.i.d.) random variables.

We use the notation:  $\mathbf{v} \sim \mathcal{N}(\mathbf{0}_{n \times 1}, \mathbf{I}_n)$ , where  $\mathbf{0}_{a \times b}$  is an  $a \times b$  matrix of zeros and  $\mathbf{I}_n$  is an  $n \times n$  identity matrix.

The least-squares (LS) estimate for the state of interest (e.g., for the vertical position coordinate, which is of primary interest in aircraft approach navigation) obtained using all available measurements is also referred to as full-set solution. It is defined as:

$$\hat{x}_0 \equiv \mathbf{s}_0^T \mathbf{z} \quad (5)$$

where  $\mathbf{s}_0$  is the  $n \times 1$  vector of LS coefficients (the same notations are used in [13]). The full-set estimate error is noted  $\varepsilon_0$ :  $\varepsilon_0 \equiv x - \hat{x}_0$ , where  $x$  is the true value of the state of interest.

### C. Solution Separation Test Statistics

A multiple-hypothesis SS RAIM method [10], [11] is adopted for detection of  $\mathbf{f}$ . A set of mutually exclusive, exhaustive hypotheses  $H_i$ , for  $i = 0, \dots, h$ , is considered. Under  $H_i$ , a number  $n_i$  of measurements is simultaneously impacted by the fault. The fault-free subset solution, which excludes these  $n_i$  measurements is written as:  $\hat{x}_i \equiv \mathbf{s}_i^T \mathbf{z}$ , where  $\mathbf{s}_i$  is the  $n \times 1$  vector of the subset solution’s LS coefficients with zeros for elements corresponding to the  $n_i$  faulted measurements [13]. SS test statistics are defined as:

$$\Delta_i \equiv \hat{x}_0 - \hat{x}_i = \mathbf{s}_i^T \mathbf{z}, \text{ for } i = 1, \dots, h,$$

where  $\Delta_i \sim \mathcal{N}(\mathbf{s}_i^T \mathbf{f}, \sigma_{\Delta_i}^2)$ , and  $\mathbf{s}_{\Delta_i} = \mathbf{s}_0 - \mathbf{s}_i$ .

The normalized SS statistics are given by:

$$q_i \equiv \Delta_i / \sigma_{\Delta_i} = \mathbf{s}_{\Delta_i}^T \mathbf{z}, \text{ for } i = 1, \dots, h \quad (6)$$

where  $\mathbf{s}_{\Delta_i} = \mathbf{s}_{\Delta_i} / \sigma_{\Delta_i}$ .

Of significance in this work is the fact that  $q_i$  can be written in terms of the parity vector, which is defined as:

$$\mathbf{p} \equiv \mathbf{Q}\mathbf{z} = \mathbf{Q}(\mathbf{v} + \mathbf{f}) \quad (7)$$

where  $\mathbf{Q}$  is the  $(n-m) \times n$  parity matrix defined as  $\mathbf{Q}\mathbf{Q}^T = \mathbf{I}_{n-m}$  and  $\mathbf{Q}\mathbf{H} = \mathbf{0}_{(n-m) \times m}$ .

For graphical representation purposes, single satellite faults (i.e.,  $n_i = 1$  and  $h = n$ ) are assumed in the first sections of this paper. Multi-satellite faults are addressed later, in Section IV-B. In this case, the test statistics  $q_i$ , for  $i = 1, \dots, h$ , can be written as [13]:

$$q_i = \mathbf{s}_{\Delta_i}^T \mathbf{z} = \mathbf{u}_i^T \mathbf{p} \quad (8)$$

where  $\mathbf{u}_i \equiv \mathbf{Q}\mathbf{A}_i (\mathbf{A}_i^T \mathbf{Q}^T \mathbf{Q}\mathbf{A}_i)^{-1/2}$ .

and  $\mathbf{A}_i^T = [\mathbf{0}_{(i-1) \times 1}^T \quad 1 \quad \mathbf{0}_{(n-i) \times 1}^T]$ ,

i.e.,  $\mathbf{Q}\mathbf{A}_i$  is the  $i^{\text{th}}$  column of  $\mathbf{Q}$  and  $\mathbf{u}_i$  is the unit direction vector of  $\mathbf{Q}\mathbf{A}_i$ , which is the direction of the  $i^{\text{th}}$  ‘fault line’ in parity space as explained below.

#### D. Illustrative Example in Parity Space

To illustrate the result in equation (8), we consider the example satellite geometry in the sky-plot in Fig. 1 where six GPS space vehicles (SVs) were in view of the user receiver. This example is used in Sections II to IV. The measurement equation (4) becomes:

$$\begin{bmatrix} \rho_1 \\ \vdots \\ \rho_6 \end{bmatrix} = \begin{bmatrix} -\mathbf{e}_1^T & 1 \\ \vdots & \vdots \\ -\mathbf{e}_6^T & 1 \end{bmatrix} \begin{bmatrix} \mathbf{x}_U \\ \tau_U \end{bmatrix} + \mathbf{v} + \mathbf{f} \quad (9)$$

where:

- $\rho_i$  for  $i=1, \dots, 6$ , are the six GPS pseudoranges
- $\mathbf{e}_i$  are the  $3 \times 1$  satellite line of sight vectors
- $\mathbf{x}_U$  is the  $3 \times 1$  user position vector in a local reference frame
- $\tau_U$  is the user receiver clock bias

Since  $m=4$  and  $n=6$ , the parity space of dimension  $(n-m)$  is two-dimensional, which is convenient for display.

In addition, the measurement noise vector is given by  $\mathbf{v} \sim \mathcal{N}(\mathbf{0}_{6 \times 1}, \mathbf{I}_6)$ , and the fault vector  $\mathbf{f}$  represents six single-SV faults, with unknown fault magnitude  $f_i$ .

$$\mathbf{f} = \left\{ \begin{bmatrix} f_1 \\ 0 \\ \vdots \\ 0 \end{bmatrix}, \begin{bmatrix} 0 \\ f_2 \\ \vdots \\ 0 \end{bmatrix}, \dots, \begin{bmatrix} 0 \\ 0 \\ \vdots \\ f_6 \end{bmatrix} \right\}$$

As shown in parity space in Fig. 2, when the fault magnitude  $f_i$  varies from  $-\infty$  to  $+\infty$ , the mean of  $\mathbf{p}$  describes a line passing through the origin with unit direction vector  $\mathbf{u}_i$ , and called the ‘fault line’. As expressed in equation (8), the SS test statistic  $q_i$  can be represented as a projection of  $\mathbf{p}$  on the  $i^{\text{th}}$  ‘fault line’ [13].

It follows that the SS RAIM detection boundary is a polygon (or a polytope in higher-dimensional parity spaces). Assuming equally-valued thresholds  $T_1 = \dots = T_6$ , Fig. 3 depicts the SS RAIM detection boundary. This boundary is shown in references [5] and [6] to approach the optimal detection region that minimizes integrity risk. SS test statistics are used in this work because they provide a computationally-efficient, practical approximation of the optimal detection region.

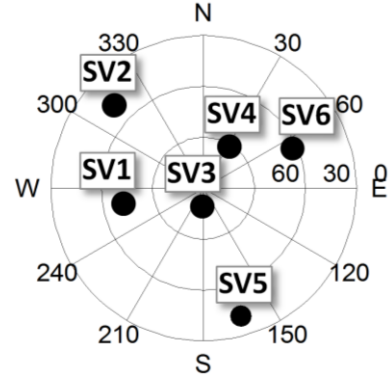


Fig. 1 Azimuth-Elevation Sky Plot For an Example Satellite Geometry

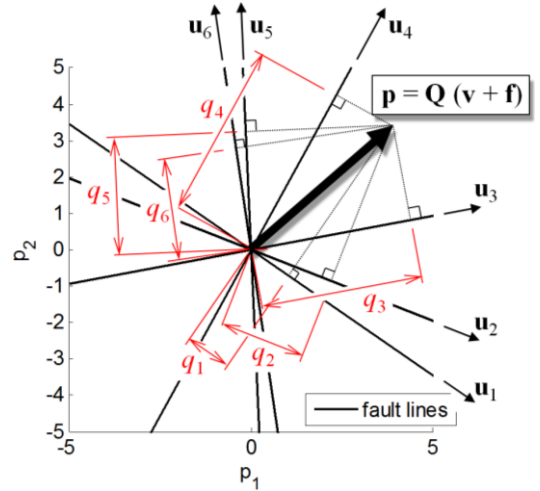


Fig. 2 Parity Space Representation of the Solution Separation Test Statistics

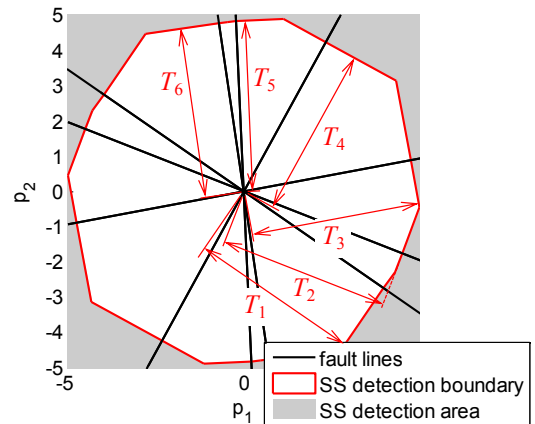


Fig. 3 Parity Space Representation of the Solution Separation Detection Boundary

Given the detector in Fig. 3, and given the LS estimator in equation (5), the integrity and continuity risk equations (2) and (3) can be expressed for conventional SS RAIM. However, simultaneously accounting for all six SS test

statistics  $q_i$ , which are all mutually correlated, would be cumbersome. In response, an upper bound  $\bar{P}_{HMI}$  on the integrity risk is derived and written as:

$$P_{HMI} = \sum_{i=0}^h \max_{f_i} P \left( \left| \varepsilon_0 \right| > \ell, \left| q_1 \right| < T_1, \dots, \left| q_h \right| < T_h \mid f_i \right) P_{Hi} \quad (10)$$

$$\leq \underbrace{\sum_{i=0}^h \max_{f_i} P \left( \left| \varepsilon_0 \right| > \ell, \left| q_i \right| < T_i \mid f_i \right) P_{Hi}}_{\equiv \bar{P}_{HMI}}$$

where the worst-case fault magnitude  $f_i$ , which maximizes integrity risk under  $H_i$ , can be determined using a straightforward line-search process [13]. Also, to avoid changing notations for the fault-free case (i.e., for the term corresponding to  $i = 0$ ), the following identity is defined:  $\{|\varepsilon_0| > \ell, |q_0| < T_0\} \equiv \{|\varepsilon_0| > \ell\}$ .

In equation (10),  $\bar{P}_{HMI}$  uses an upper bound on the probability of no-detection:

$$P(|q_1| < T_1, \dots, |q_6| < T_6 | H_i) \leq P(|q_i| < T_i | f_i) \quad (11)$$

This probability is represented in Fig. 4 under  $H_1$ , i.e., assuming a fault on SV 1: the actual no detection probability given on the left-hand-side in equation (11) is the probability of  $\mathbf{p}$  being inside the red detection boundary in Fig. 4. Evaluating the probability of being within this complex polygon would be tedious. Instead, the bound on the right-hand-side in equation (11) expresses the probability of being within the gray band in Fig. 4, which is easy to compute. This integrity risk bound is conservative, but remains relatively tight because most of the probability density is concentrated around the fault line (which represents the mean of  $\mathbf{p}$  for varying fault magnitudes).

Additional bounding steps are typically implemented in conventional SS RAIM [10], [11]. These steps are fully detailed in [13], and will be used later in Section IV-B.

In parallel, a continuity risk bound is established, and given by:

$$P_{FA} = P \left( |q_1| \geq T_1 \cup \dots \cup |q_6| \geq T_6 \mid H_0 \right) P_{H0} \quad (12)$$

$$\leq \sum_{i=1}^h P \left( |q_i| \geq T_i \mid H_0 \right) P_{H0}$$

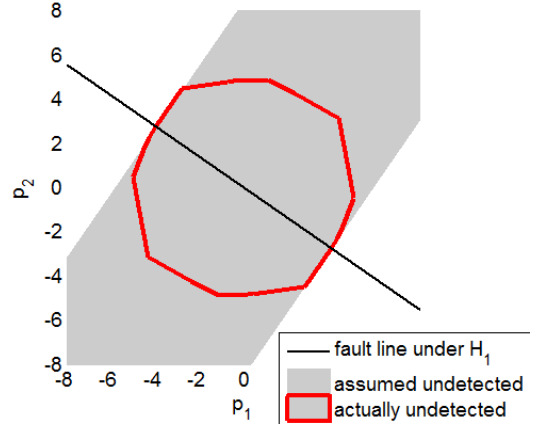


Fig. 4 Parity Space Representation of the First Step in the SS RAIM Integrity Risk Bound

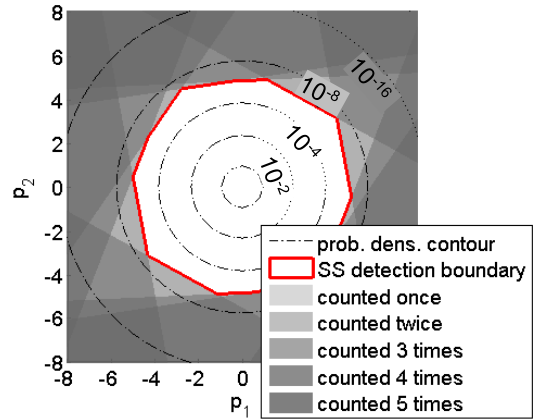


Fig. 5 Parity Space Representation of the SS RAIM Continuity Risk Bound

The actual probability of false alarm is the probability of  $\mathbf{p}$  being outside the detection boundary when the mean of  $\mathbf{p}$  is  $\mathbf{0}_{2 \times 1}$ . In Fig. 5, lines of constant probability density are displayed under  $H_0$ . In this case again, evaluating the probability of being outside the red boundary would be tedious. Instead, the easy-to-compute bound on the right-hand-side of the inequality in equation (12) can be represented as counting multiple times the probabilities of  $\mathbf{p}$  being in the areas with different shades of gray, as indicated in Fig. 5. This approach is conservative, but not overly-conservative since the probability density levels under  $H_0$  are extremely low outside the detection boundary.

Equation (12) is used to determine the detection thresholds  $T_i$ , for  $i=1, \dots, 6$ . Thresholds  $T_i$  are set to limit the probability of false alarm, for example, following the equation:  $T_i = Q^{-1}\{C_{REQ}/(2hP_{H0})\}$  where the function  $Q^{-1}\{\}$  is the inverse tail probability of the

standard normal distribution, and in this case, the number of fault hypotheses is six ( $h=6$ ).

The remainder of the paper aims at designing new NLS estimators. Since the estimator does not impact the continuity risk, the focus is placed on minimizing the integrity risk in equation (10).

### III. NON-LEAST-SQUARES ESTIMATOR DESIGN TO MINIMIZE INTEGRITY RISK

This section describes a method to find the optimal estimator that minimizes integrity risk. This first method will be computationally expensive, but provides the best achievable integrity performance. It will be used as a starting point in Section IV to derive an estimator design procedure requiring much shorter processing times.

#### A. Direct Integrity Risk Evaluation (DIRE) Using a Non-Least-Squares (NLS) Estimator

As mentioned Section I, three main research efforts have investigated the possibility of using non least squares (NLS) estimators in RAIM [7], [8], [9]. This section builds upon the work by Blanch et al. in [9]. However, in contrast with [9], the method described here enables direct integrity risk evaluation (DIRE) instead of using protection level (PL) equations. DIRE provides tighter integrity risk bounds than PL [13].

The NLS estimate for the state of interest  $\hat{x}_{NLS}$  can be written as a sum of two orthogonal components of the measurement vector  $\mathbf{z}$  :

$$\hat{x}_{NLS} \equiv \mathbf{s}_0^T \mathbf{z} + \boldsymbol{\beta}^T \mathbf{Q} \mathbf{z} \quad (13)$$

where

$\mathbf{s}_0^T \mathbf{z}$  is the state estimate in equation (5), which lies in the column space of  $\mathbf{H}$   
 $\boldsymbol{\beta}^T \mathbf{Q} \mathbf{z}$  lies in the parity space, or left null space of  $\mathbf{H}$   
 $\boldsymbol{\beta}$  is the  $(n-m) \times 1$  design parameter vector also called ‘estimator modifier’

This section presents a method to determine the vector  $\boldsymbol{\beta}$  that minimizes integrity risk.

Substituting equation (4) into (13), and using the definition of  $\mathbf{Q}$ , shows that the estimator is unbiased, so that the NLS state estimate error can be written independently of  $x$  as:

$$\varepsilon_{NLS} \equiv \hat{x}_{NLS} - x = (\mathbf{s}_0^T + \boldsymbol{\beta}^T \mathbf{Q})(\mathbf{v} + \mathbf{f}) \quad (14)$$

Integrity risk evaluation is carried out using equation (10), but the estimate error  $\varepsilon_{NLS}$  replaces  $\varepsilon_0$ . Because  $\varepsilon_{NLS}$  is not derived from a LS estimator,  $\varepsilon_{NLS}$  and  $q_i$  are correlated [13]. In this case, the joint probabilities in equation (10) cannot be evaluated as products of probabilities. Fortunately, numerical methods are available to compute joint probabilities for multi-variate normally distributed random vectors [16]. These methods are computationally expensive, which will be addressed in Section IV.

The estimate error  $\varepsilon_{NLS}$  and the test statistic  $q_i$  can be arranged in a bivariate normally distributed random vector defined as:

$$\boldsymbol{\eta}_i \equiv [\varepsilon_{NLS} \quad q_i]^T \quad \text{and} \quad \boldsymbol{\eta}_i \sim \mathcal{N}(\boldsymbol{\mu}_{\eta_i}, \mathbf{P}_{\eta_i}) \quad (15)$$

where

$$\boldsymbol{\mu}_{\eta_i} = \begin{bmatrix} \mathbf{s}_0^T + \boldsymbol{\beta}^T \mathbf{Q} \\ \mathbf{u}_i^T \mathbf{Q} \end{bmatrix} \mathbf{f} \quad \text{and} \quad \mathbf{P}_{\eta_i} = \begin{bmatrix} \sigma_0^2 + \boldsymbol{\beta}^T \boldsymbol{\beta} & \boldsymbol{\beta}^T \mathbf{u}_i \\ \mathbf{u}_i^T \boldsymbol{\beta} & 1 \end{bmatrix} \quad (16)$$

where equations (7) and (8) were used to express the test statistic  $q_i$ .

The impact of the estimator modifier vector  $\boldsymbol{\beta}$  is illustrated in a ‘failure mode plot’ in Fig. 6, for the example six-satellite geometry displayed in Fig. 1, under hypothesis  $H_5$  of a fault on SV 5. To analyze the impact of  $\boldsymbol{\beta}$ , the new NLS-estimator-based method is compared to the conventional RAIM method using the LS estimator, for which  $\boldsymbol{\beta} = \mathbf{0}_{(n-m) \times 1}$ . In Fig. 6, the estimate error  $\varepsilon$  is displayed versus test statistic  $q_5$ . The notation ‘ $\varepsilon$ ’ designates both  $\varepsilon_0$  for the LS estimator, and  $\varepsilon_{NLS}$  for the NLS estimator. Conventional RAIM is represented using dashed lines, whereas dark-gray color and solid lines are employed for the new method using the NLS estimator. Both methods are evaluated assuming the measurement model in equation (9), and assuming a prior probability of fault  $P_{Hi}$ , for  $i \neq 0$ , of  $10^{-4}$ .

Example navigation requirements include a continuity risk requirement  $C_{REQ}$  of  $8 \cdot 10^{-6}$ , and an alert limit  $\ell$  of 15 m. The alert limit  $\ell$  and the detection threshold  $T_5$  define the boundaries of the HMI area in the upper left-hand quadrant (shadowed in light red). Under  $H_5$ , as the fault magnitude varies, the means of  $\varepsilon$  and of  $q_5$  describe a ‘fault line’ passing through the origin, with slope  $g_{0,5}$  for the LS estimator, and  $g_{NLS,5}$  for the NLS estimator. For a given fault magnitude, lines of constant

joint probability density are represented. These contours are ellipses because  $\varepsilon$  and  $q_5$  are normally distributed. The ellipses are labelled in terms of  $-\log_{10} f_{\eta_i}(\varepsilon, q_i)$ , where:

$$f_{\eta_i}(\varepsilon, q_i) \equiv \frac{1}{2\pi \det(\mathbf{P}_{\eta_i})} \exp\left(-\frac{1}{2}(\boldsymbol{\eta}_i - \boldsymbol{\mu}_{\eta_i})^T \mathbf{P}_{\eta_i}^{-1}(\boldsymbol{\eta}_i - \boldsymbol{\mu}_{\eta_i})\right)$$

The  $10^{-2}$  joint probability density level is emphasized for illustration purposes. The probability of being in the HMI area is the integrity risk given  $H_5$ .

For the LS estimator,  $\varepsilon_0$  and  $q_i$  are statistically independent [13], so that the major axis of the dashed ellipse is either horizontal, or vertical. In contrast, using a NLS estimator provides the means to move the dark ellipse away from the HMI area, hence reducing the integrity risk. The influence of the estimator modifier vector  $\boldsymbol{\beta}$  is threefold.

- The fact that  $\boldsymbol{\beta}$  impacts the mean of  $\varepsilon_{NLS}$  (in equations (16)) enables reduction of the failure mode slope from  $g_{0,i}$  to  $g_{NLS,i}$ , which lowers integrity risk.
- Off-diagonal components of the covariance matrix  $\mathbf{P}_{\eta_i}$  also vary with  $\boldsymbol{\beta}$  so that the dark ellipse's orientation can be modified.
- However,  $\boldsymbol{\beta}$  causes the diagonal element of  $\mathbf{P}_{\eta_i}$  corresponding to  $\varepsilon_{NLS}$  to increase, which means that the dark ellipse is inflated along the  $\varepsilon$ -axis in Fig. 6. This negative aspect will be accounted for in the integrity risk evaluation. The increase in variance of  $\varepsilon_{NLS}$  also explains that lowering integrity risk comes at the cost of a decrease in accuracy performance.

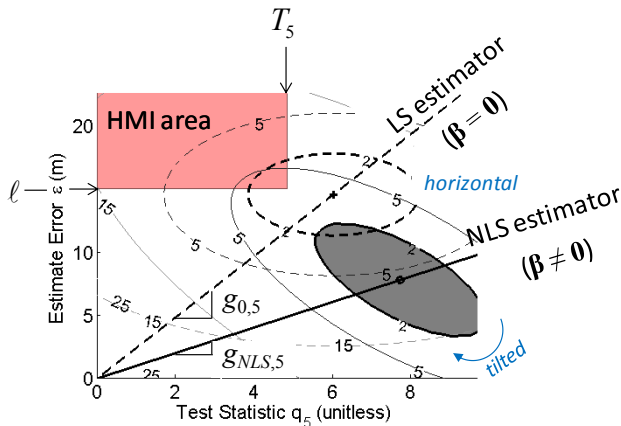


**Fig. 6 Failure Mode Plot of LS Versus NLS Estimator-Based RAIM, Assuming a Fault on SV 5.**

Figure 6 only considers one fault hypothesis  $H_5$ . But, the estimator modifier vector  $\boldsymbol{\beta}$  must be determined to minimize the overall integrity risk, considering all hypotheses  $H_i$ , for  $i=0, \dots, h$  as defined in equation (10).

### B. Multi-Dimensional Optimization (MDO).

The problem of finding the  $(n-m) \times 1$  vector  $\boldsymbol{\beta}$  that minimizes the overall integrity risk can be mathematically formulated using the bound  $\bar{P}_{HMI}$  defined in equation (10) as:  $\min_{\boldsymbol{\beta}} \bar{P}_{HMI}$ . An equivalent expression is given by:

$$\min_{\boldsymbol{\beta}} \sum_{i=0}^h \left[ \int_{-\infty}^{-T_i} \int_{-T_i}^{T_i} f_{\eta_i}(\varepsilon_{NLS}, q_i) dq_i d\varepsilon_{NLS} + \int_{T_i}^{+\infty} \int_{-T_i}^{T_i} f_{\eta_i}(\varepsilon_{NLS}, q_i) dq_i d\varepsilon_{NLS} \right] P_{H_i} \quad (17)$$

This multi-dimensional optimization (MDO) problem (i.e., finding the  $(n-m)$  elements of  $\boldsymbol{\beta}$ ) can be solved numerically using a modified Newton method (e.g., see [17]). The gradient and Hessian of the objective function in Equation (11) can be established numerically using procedures given in [17]. This process is again computationally intensive. Computational efficiency is addressed later in Section IV.

The minimization process outputs an estimator modifier vector  $\boldsymbol{\beta}$ . A failure mode plot is used again in Fig. 7 to analyze  $\boldsymbol{\beta}$ , but in contrast with Fig. 6, all six single-SV fault hypotheses are simultaneously represented. In Fig. 7, ellipses corresponding to the  $10^{-2}$  joint probability density level are displayed with dashed black lines for the LS estimator (labeled DIRE LS), and with grey shadowed areas for the NLS estimator (labeled DIRE MDO because  $\boldsymbol{\beta}$  is obtained from a MDO). Figure 7 shows one ellipse for DIRE LS overlapping the HMI area, whereas none of the grey-shadowed ellipses for DIRE MDO does.

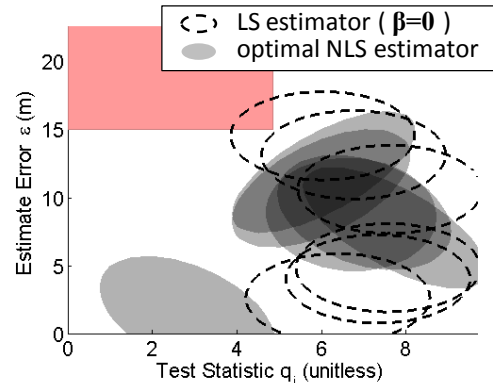


**Fig. 7 Failure Mode Plot Displaying all Single-SV Fault Hypotheses**

In this example, the integrity risk decreases from  $4.7 \cdot 10^{-6}$  for the LS estimator to  $3.6 \cdot 10^{-8}$  using the DIRE MDO method. The price to pay for this integrity risk reduction is an increase in the vertical position estimate standard deviation from 1.49 m using DIRE LS to 2.02 m using DIRE MDO (further analysis of the positioning standard deviation is carried out in Section V).

These results show that using a NLS estimator in RAIM can dramatically reduce the integrity risk. The integrity risk obtained using DIRE MDO is deemed the lowest achievable risk, under the continuity risk constraint given in equation (12). However, the multi-dimensional optimization process used to determine  $\beta$  is extremely time intensive. In Section IV, the DIRE MDO method is modified to reduce the computation load.

#### IV. PRACTICAL APPROACH TO NON-LEAST-SQUARES ESTIMATOR DESIGN

This section uses a parity space representation to establish an approximation of the optimal estimator modifier vector  $\beta$  using a one-dimensional optimization (ODO) process instead of the multi-dimensional optimization (MDO) procedure described in Section III. Further reduction in computation load is accomplished using an integrity risk bound (IB) rather than performing direct integrity risk evaluation (DIRE).

##### A. One-Dimensional Optimization (ODO).

The focus of this derivation is on the  $n$  single-SV faults. Multi-SV faults are addressed in Section IV-B. Under a single-SV fault hypothesis  $H_i$ , the fault vector is expressed as:  $\mathbf{f}_i = \mathbf{A}_i f_i$ , where  $f_i$  is the fault magnitude, and  $\mathbf{A}_i$  is defined under equation (8). Substituting the above expression of  $\mathbf{f}_i$  for  $\mathbf{f}$  into equation (16) and simplifying the result, equation (16) becomes:

$$\mu_{\eta} = \begin{bmatrix} g_{0,i} + \beta \rho_{\beta,i} \\ 1 \end{bmatrix} f_{i*} \text{ and } \mathbf{P}_{\eta} = \begin{bmatrix} \sigma_0^2 + \beta^2 & \beta \rho_{\beta,i} \\ \beta \rho_{\beta,i} & 1 \end{bmatrix} \quad (18)$$

where

$$\beta^2 = \beta^T \beta, \quad \rho_{\beta,i} = \mathbf{u}_{\beta}^T \mathbf{u}_i \text{ with } \mathbf{u}_{\beta} = \beta / \beta \quad (19)$$

$$f_{i*} = \sqrt{\mathbf{A}_i^T \mathbf{Q}^T \mathbf{Q} \mathbf{A}_i} f_i, \quad g_{0,i} = \frac{\mathbf{s}_0^T \mathbf{A}_i}{\sqrt{\mathbf{A}_i^T \mathbf{Q}^T \mathbf{Q} \mathbf{A}_i}} = \sigma_{\Delta i} \quad (20)$$

In the above equations,  $\beta$  and  $\mathbf{u}_{\beta}$  respectively designate the magnitude and unit direction vector of  $\beta$ . Also, it was

shown in [13] that  $g_{0,i}$  could be written as:  $g_{0,i} = \sigma_{\Delta i}$ , where  $\sigma_{\Delta i}$  was defined in the paragraph above equation (6).

The optimal  $(n-m) \times 1$  vector  $\beta$  obtained using DIRE MDO is displayed in red in parity space in Fig. 8 for the example six-SV geometry introduced in Fig. 1. Single-SV fault lines are represented in dashed gray. In parallel, consider the maximum fault mode slope  $\max_{i=1,\dots,n} \{g_{0,i}\}$  for the LS estimator, which is shown in solid blue in Fig. 9 (and corresponds to a fault on SV 5). The fault line corresponding to this maximum slope  $\max_{i=1,\dots,n} \{g_{0,i}\}$  is also represented in solid blue in Fig. 8.

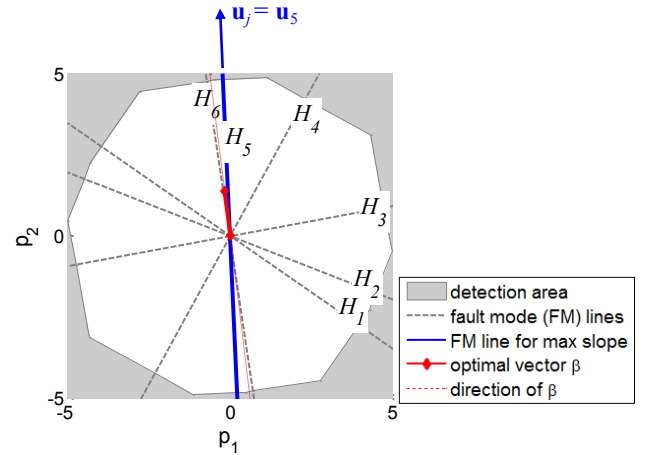


Fig. 8 Comparison of DIRE MDO Vector  $\beta$  Versus Worst-Case Fault Line Directions in Parity Space

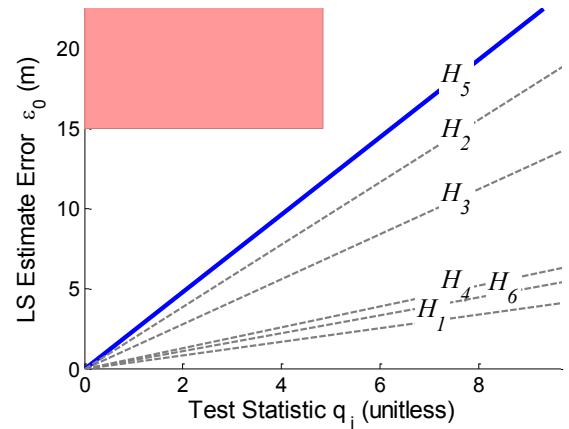


Fig. 9 Failure Mode Plot Showing Failure Mode Lines for All Six Single-Satellite Fault Modes



Let  $\mathbf{u}_j$  be the unit direction vector in parity space of the fault line corresponding to  $\max_{i=1,\dots,n} \{g_{0,i}\}$  (in this case,  $\mathbf{u}_j = \mathbf{u}_5$ ). Fig. 8 shows that the direction of the optimal  $\beta$  vector in parity space is very close to that of  $\mathbf{u}_5$ . The same observation was made for many other satellite geometries.

Few examples were found, where the optimal  $\beta$  direction does not match  $\mathbf{u}_j$ . These examples occur when the second largest failure mode slope approaches  $\max_{i=1,\dots,n} \{g_{0,i}\}$ . In these cases, the optimal  $\beta$ -direction is somewhere between the directions of the two fault lines for these two dominating fault modes. For most other geometries, the maximum fault slope is an outlier-slope, i.e., is much larger than the other  $n-1$  single-SV slopes. Therefore, in the vast majority of cases, the direction of the optimal  $\beta$  vector in parity space matches the direction of  $\mathbf{u}_j$ .

It follows from the analysis in Fig. 8, that a reasonable simplification relative to MDO is to approximate the optimal  $\beta$  vector as:  $\beta = -\beta \mathbf{u}_j$ , where  $j = \arg \max_{i=1,\dots,n} g_{0,i}$ . (The minus sign is included so that only positive values of  $\beta$  need to be considered.) The estimator modifier vector  $\beta$  can now be determined by finding the value of  $\beta$ , which minimizes the integrity risk, i.e., by solving equation (17) over the scalar parameter  $\beta$  instead of over vector  $\beta$ . This is a one-dimensional optimization (ODO) process that can be performed using a straightforward line search routine.

It is worth noting that an approximation of the optimal  $\beta$ -direction is sufficient to guarantee that the NLS estimator will perform equally or better than the LS estimator, because the search over  $\beta$  includes the value  $\beta=0$ , for which LS and NLS estimators are identical.

Moreover, the search over  $\beta$  can be limited to ensure that the accuracy requirement is satisfied: accuracy is directly related to the variance  $\sigma_{NLS}^2$  of  $\varepsilon_{NLS}$  (in equation (18),  $\sigma_{NLS}^2 = \sigma_0^2 + \beta^2$ ). For example, if the accuracy limit is noted  $\ell_{ACC}$ , then the 95% accuracy criterion is:  $2\sigma_{NLS} < \ell_{ACC}$ , which is equivalent to:  $\beta < (\ell_{ACC}^2 / 4 - \sigma_0^2)^{1/2}$ .

With this choice of  $\mathbf{u}_\beta$  (as  $\mathbf{u}_\beta = -\mathbf{u}_j$ ), an equivalent expression for the NLS estimator is obtained using equation (8):

$$\hat{\mathbf{x}}_{NLS} \equiv \mathbf{s}_0^T \mathbf{z} - \beta \mathbf{s}_{\Delta j}^T \mathbf{z},$$

or equivalently,

$$\hat{\mathbf{x}}_{NLS} = \mathbf{s}_0^T \mathbf{z} - \beta_* \mathbf{s}_{\Delta j}^T \mathbf{z} \quad \text{where} \quad \beta_* \equiv \beta / \sigma_{\Delta j} \quad (21)$$

Thus the minimization problem in equation (17) can fully be expressed in terms of scalars and vectors already used in SS RAIM: matrix  $\mathbf{Q}$  does not need to be computed. For example,  $\rho_{\beta,i}$  in Equation (19) becomes  $\rho_{\beta,i} = -\mathbf{s}_{\Delta j}^T \mathbf{s}_{\Delta i} / (\sigma_{\Delta j} \sigma_{\Delta i})$ , and using equation (20),  $f_{i*}$  can be written in terms of:  $(\mathbf{A}_i^T \mathbf{Q}^T \mathbf{Q} \mathbf{A}_i)^{1/2} = \sigma_{\Delta i} / \mathbf{s}_0^T \mathbf{A}_i$ .

In an independent study soon to be published in [18], a similar choice was made for the NLS estimator design. The algorithm derivation in [18] is fully carried out in the position domain, which makes it barely recognizable from the above method. But the fundamental underlying principle which, in our interpretation, steer the choice of  $\mathbf{u}_\beta$ , is identical.

Figure 10 shows that, for the example used in Fig. 1 to 9, DIRE ODO matches DIRE MDO very closely. The integrity risk only increases from  $3.6 \cdot 10^{-8}$  to  $5.1 \cdot 10^{-8}$  for MDO versus ODO, which is still a dramatic reduction as compared to the  $4.7 \cdot 10^{-6}$  value obtained using DIRE LS. In addition, DIRE ODO is computationally much more efficient than DIRE MDO. Despite this improvement in run time, the DIRE method is still not fit for real time implementations, mainly because the process involves integration in equation (17) of the bivariate normal density functions of  $\eta_i$ , for  $i=1,\dots,h$  (run-time will be quantified in Section V). In response, an integrity risk bound (IB) is derived.

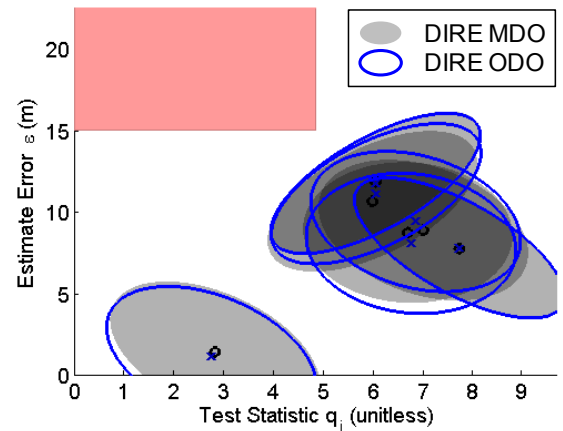


Fig. 10 Failure Mode Plot Comparing DIRE MDO Versus DIRE ODO

### B. Integrity Risk Bounding Method (IB).

In parallel to the minimization problem over the estimator modifier  $\beta$ , the direct integrity risk evaluation (DIRE) method includes two other time-consuming steps: (a) the integration of the bivariate normal distribution of vector  $\boldsymbol{\eta}_i = [\varepsilon_{NLS} \quad q_i]^T$  in equation (17), and (b) the scalar search for worst-case magnitude  $f_i$  expressed in equation (10). Both points are addressed using integrity risk bounds (IB), which are looser than using DIRE, but are much faster to evaluate.

First, it is worth reminding that the integration of bivariate normal distributions was needed to evaluate the integrity risk in equation (17) because  $\varepsilon_{NLS}$  and  $q_i$  are correlated. To avoid dealing with bivariate normal distributions, a bound on the integrity risk in equation (10) is established using conditional probabilities as follows:

$$\begin{aligned} \bar{P}_{HMI} &\leq \sum_{i=0}^h \max_{f_i} \left[ P(\varepsilon_{NLS} > \ell \mid f_i, |q_i| < T_i) \right. \\ &\quad \left. \times P(|q_i| < T_i \mid f_i) P_{Hi} \right] \\ &\leq \sum_{i=0}^h \max_{f_i} P(\varepsilon_{NLS} > \ell \mid f_i, |q_i| < T_i) P_{Hi} \end{aligned} \quad (22)$$

where ‘ $\times$ ’ designates a (scalar) multiplication. It was shown in [13] that the bound  $P(|q_i| < T_i \mid H_i) = 1$  in the last inequality could be loose. This upper bound is conventionally used in SS RAIM [10], [11] (although not explicitly), and is the price to pay to significantly reduce the processing time.

Second, in order to evaluate the above expression independently of fault magnitude  $f_i$ , the estimation error for  $\hat{x}_{NLS}$  in equation (21) is expressed as:

$$\varepsilon_{NLS} = (\mathbf{s}_0^T - \beta_* \mathbf{s}_{Nj}^T) \mathbf{z} = \mathbf{s}_i^T \mathbf{v} + (\mathbf{s}_{\Delta i}^T - \beta_* \mathbf{s}_{Nj}^T) (\mathbf{v} + \mathbf{f}_i) \quad (23)$$

where

- $\mathbf{s}_0$  is written as:  $\mathbf{s}_0 = \mathbf{s}_i + \mathbf{s}_0 - \mathbf{s}_i$ ,
- $\mathbf{s}_{\Delta i}$  is defined above equation (6) as:  $\mathbf{s}_{\Delta i} = \mathbf{s}_0 - \mathbf{s}_i$
- $\mathbf{f}_i$  is defined above equation (18),
- $\beta_*$  is defined in equation (21),
- $\mathbf{s}_i^T \mathbf{f}_i = \mathbf{0}$  under  $H_i$ .

The term  $(\mathbf{s}_{\Delta i}^T - \beta_* \mathbf{s}_{Nj}^T) (\mathbf{v} + \mathbf{f}_i)$  is a function of the fault  $\mathbf{f}_i$ . To eliminate this dependency, a *new, sub-optimal detection test statistic* is considered:

$$\Delta_{NLSi} \equiv (\mathbf{s}_{\Delta i}^T - \beta_* \mathbf{s}_{Nj}^T) \mathbf{z} = (\mathbf{s}_{\Delta i}^T - \beta_* \mathbf{s}_{Nj}^T) (\mathbf{v} + \mathbf{f}_i) \quad (24)$$

The variance of  $\Delta_{NLSi}$  can be written as:

$$\sigma_{\Delta NLSi}^2 = \sigma_{\Delta i}^2 - 2\mathbf{s}_{\Delta i}^T \mathbf{s}_{Nj} \beta_* + \beta_*^2 \sigma_{Nj}^2. \quad (25)$$

and the detection threshold for  $\Delta_{NLSi}$  is defined as:  $T_{\Delta NLSi} \equiv T_i \sigma_{\Delta NLSi}$ . Using  $\Delta_{NLSi}$  instead of  $q_i$ , substituting (24) into (23) and the result into (22), and using the condition in (22) (which is rewritten as  $|\Delta_{NLSi}| < T_{\Delta NLSi}$ ), the following integrity risk bound is obtained:

$$\begin{aligned} P_{HMI} &\leq P(\varepsilon_{NLS} > \ell \mid H_0) P_{H0} \\ &\quad + \sum_{i=1}^h P(|\varepsilon_i| + T_{\Delta NLSi} > \ell \mid H_i) P_{Hi} \equiv \bar{P}_{HMI} \end{aligned} \quad (26)$$

It is worth noting that equation (26) can be evaluated for both single-SV and multi-SV faults, since all SS RAIM variables and parameters (including  $\varepsilon_i$ ,  $\sigma_{\Delta i}$ , and  $\mathbf{s}_{\Delta i}$ ) were defined in Section II-C assuming that subsets of one or more measurements could simultaneously be faulted.

Equation (26) is then exploited in the integrity risk bounding process using one-dimensional optimization, also called the ‘IB ODO’ method. Scalar  $\beta_*$  is found by solving:

$$\min_{\beta_*} \{\bar{P}_{HMI}\} \quad (27)$$

If required, and as described in the paragraph above equation (21), the search over  $\beta_*$  can be limited by the accuracy criterion to the following range of values:  $0 \leq \beta_* < (\ell_{ACC}^2 / 4 - \sigma_0^2)^{1/2} / \sigma_{Nj}$ .

Given vector  $\beta$  (expressed in parity space as  $\beta = -\beta_* \sigma_{Nj} \mathbf{u}_j$ ), the new detection test statistic  $\Delta_{NLSi}$  departs from the LS SS statistic  $q_i$  (or equivalently from  $\Delta_i = q_i \sigma_{\Delta i}$ ). In Fig. 11, the detection boundaries derived from  $\Delta_{NLSi}$  (represented with a thick red contour) and  $q_i$  (gray shadowed area) are compared in parity space, for the example satellite geometry presented in Fig. 1. The difference in the resulting detection regions further explains that the integrity risk bound using this IB procedure is looser than using DIRE. (Recall that  $q_i$  used in DIRE was shown in [5] and [6] to approach the optimal test statistic.) But IB ODO requires significantly less computation resources than when DIRE MDO. This comparison is quantified in Section V.

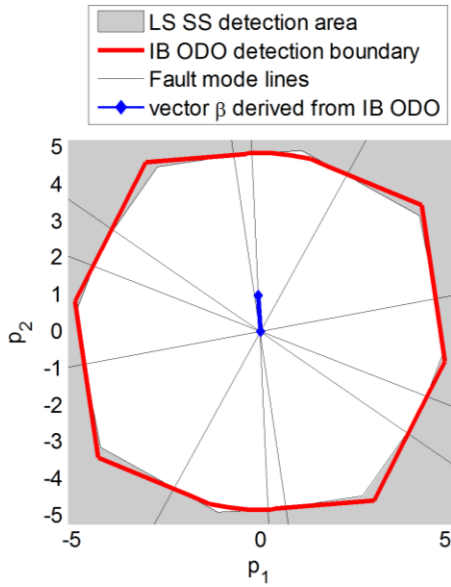


Fig. 11 Detection Region for LS SS Versus the Integrity Risk Bounding (IB) Method

## V. AVAILABILITY AND COMPUTATION TIME EVALUATION

This section aims at analyzing the integrity risk reduction and increase in processing time generated when implementing a NLS estimator as compared to using a LS estimator in SS RAIM. The algorithms derived in Sections II to IV are evaluated in an example Advanced RAIM (ARAIM) application for vertical guidance of aircraft using dual-frequency GPS and Galileo. The simulation parameters, which include ARAIM measurement error models, and LPV-200 navigation requirements (to support localizer precision vertical aircraft approach operations down to 200 feet above the ground), are listed in Table 1 and described in detail in [3]. In this analysis, two major differences with respect to the ARAIM error models are that constellation-wide faults are not accounted for, and that fault-free measurement biases are assumed to be zero. These biases introduce application-specific complications whose treatment is not relevant to this paper. To simplify the analysis, accuracy requirements were not included in the availability assessment (but can easily be incorporated in the  $\beta$  determination process as described in Section IV).

Example navigation requirements include an integrity risk requirement  $I_{REQ}$  of  $10^{-7}$ , and a continuity risk requirement  $C_{REQ}$  of  $10^{-6}$ . The prior probability of satellite fault  $P_{Hi}$  is assumed to be  $10^{-5}$ . The alert limit  $\ell$  is reduced from 35 m in ARAIM [3] to 10 m in this performance evaluation. A ‘24-1’ GPS satellite constellation and a ‘27-1’ Galileo constellation are assumed, which are nominal constellations with one

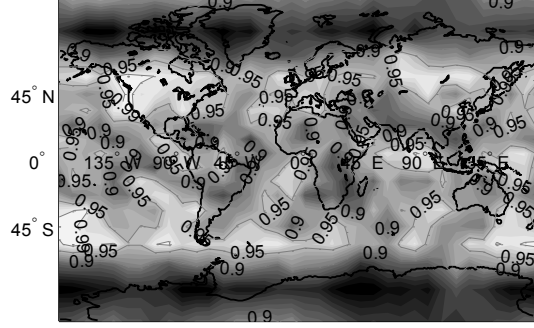
spacecraft removed to account for outages; these example constellations are also described in [3]. Moreover, this analysis focuses on the vertical position coordinate, for which the aircraft approach navigation requirements are often the most difficult to fulfill.

Figures 12 to 14 display availability maps for a  $10 \text{ deg} \times 10 \text{ deg}$  latitude-longitude grid of locations, for GPS/Galileo satellite geometries simulated at regular five minute intervals over a 24 hour period. Availability is computed at each location as the fraction of time where the  $P_{HMI}$ -bound meets  $I_{REQ}$ . In the figures, availability is color-coded: white color corresponds to a value of 100%, black represents 80%. Constant availability contours are also displayed. The worldwide availability metric given in figure captions is the average over all grid points of the availability weighted by the cosine of the latitude, because grid point locations near the equator represent larger areas than near the poles.

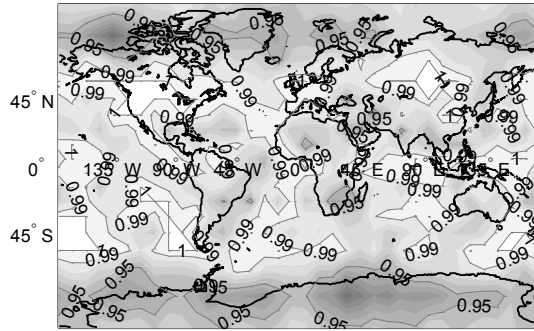
Figure 12 presents availability for the integrity risk bounding (IB) method using a LS estimator, i.e., using a conventional SS RAIM method [10], [11] (with optimal integrity risk allocation since a  $P_{HMI}$ -bound is used rather than protection levels). Then, Fig. 13 displays the availability provided by direct integrity risk evaluation (DIRE) using a one-dimensional optimization (ODO) process to determine the NLS estimator. The DIRE multi-dimensional optimization (MDO) would probably have generated slightly higher availability, but the computation time to generate an availability map would have exceeded several months. Thus, the 98.1% worldwide average availability value for DIRE ODO is our closest approximation of the best availability that can be reached using a NLS estimator. Finally, the availability map for the computationally-efficient IB ODO method is shown in Figure 14. Average availability using IB ODO is 96.7%, which does not quite reach the best achievable 98.1% availability, but is still much higher than the 92.6% value obtained using a LS estimator in Figure 12.

Table 1. Simulation Parameters

| Description (standard deviations)                     | Value   |
|---|---|
| SV clock and orbit error (URA)                        | 0.75 m<br>(0.957 m for Galileo)   |
| Residual tropospheric error *                         | $0.12 \frac{1.001}{(0.002001 + \sin^2 \xi)^{1/2}} \text{ m}$            |
| Smoothed code multipath *                             | $0.13 + 0.53e^{-\xi/10} \text{ m}$<br>(lookup table for Galileo in [3]) |
| Smoothed code receiver noise *                        | $0.15 + 0.43e^{-\xi/6.9} \text{ m}$                                     |
| *: $\xi$ is the satellite elevation angle in degrees. |   |



**Fig. 12 Availability Map for Integrity Risk Bounding Method (IB) Using a Least Squares Estimator (LS): Worldwide Weighted Average Availability is 92.6%**



**Fig. 13 Availability Map for Direct Integrity Risk Evaluation Using One-Dimensional Optimization (DIRE ODO): Worldwide Weighted Average Availability is 98.1%**

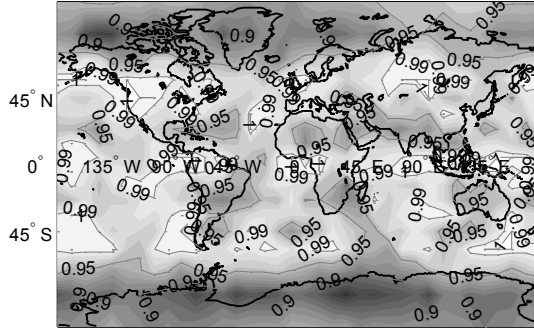


**Fig. 14 Availability Map for Integrity Risk Bounding Using One-Dimensional Optimization (IB ODO): Worldwide Weighted Average Availability is 96.7%**

Average availability numbers are listed in Table 2 for conventional RAIM using a LS estimator (labeled IB LS), for the method giving the best achievable performance (DIRE ODO), and for the computationally-efficient approach (IB ODO). The third column of Table 2 shows

the inflation of the vertical position estimate standard deviation caused by the use of a NLS estimator rather than a LS estimator. This factor  $\sigma_{NLS} / \sigma_0$  can cause the accuracy performance to diminish, but for all algorithms, the inflation factor averaged over all locations and satellite geometries remains lower than 1.03. Also, as mentioned in Section IV, the accuracy requirement can be built into the NLS estimator design algorithm to ensure that the accuracy criterion remains satisfied when it is initially met for the LS estimator.

The fourth column in Table 2 gives the inflation in computation time for each algorithm as compared to the IB LS computation time. The reference IB LS run time is 0.8 ms per geometry. These numbers were generated on a computer equipped with a 3.40GHz Intel(R) Core(TM) i7-2600 processor and 8 GB RAM. Computation times can be analyzed in parallel with worldwide average availability results in the second column of Table 2. The DIRE ODO achieves 98.1% availability, but the run time inflation factor is almost 2000. The IB ODO method accomplishes an effective compromise between run time and availability performance: availability using IB ODO increases by 4.1% with respect to IB LS, but the run time is only about twice that of IB LS.

## VI. CONCLUSION

This paper describes new methods to minimize the integrity risk by design of the RAIM estimator, for applications in future multi-constellation global navigation satellite systems (GNSS).

The first method based on direct integrity risk evaluation (DIRE), aims at minimizing integrity risk regardless of computation load, and provides a measure of the best achievable integrity performance. This method is computationally expensive. As an alternative, a second method based on integrity risk bounding, using one-dimensional optimization (IB ODO) is developed using parity space representations and failure mode plots. Despite conservative assumptions in the integrity risk bounding process, IB ODO still significantly lowers integrity risk as compared to using a least-squares (LS) estimator, but also considerably reduces processing load with respect to DIRE.

**Table 2. Simulation Results**

|          | Average availability | Average $\sigma_{NLS} / \sigma_0$ | Run time Inflation w.r.t. IB LS |
|----------|----------------------|-----------------------------------|---------------------------------|
| IB LS    | 92.6%                | 1                                 | 1                               |
| DIRE ODO | 98.1%                | 1.01                              | 1889                            |
| IB ODO   | 96.7%                | 1.03                              | 2.4                             |

Performance analyses are carried out for an example aircraft approach application using multi-constellation Advanced RAIM. For a given set of navigation system parameters, the worldwide average availability provided by IB ODO is slightly lower than the best achievable performance (evaluated using DIRE), but is substantially higher than using a LS estimator. In addition, IB ODO does not significantly degrade the accuracy performance as compared to a LS estimator. Finally, the IB ODO processing time is almost 1000 times shorter than for DIRE, and is only about twice that of a conventional LS SS RAIM algorithm, which may enable real time implementation in applications where computation resources are limited.

## ACKNOWLEDGMENTS

The authors would like to thank the Federal Aviation Administration for sponsoring this work.

## REFERENCES

- [1] Lee, Y. C., "Analysis of Range and Position Comparison Methods as a Means to Provide GPS Integrity in the User Receiver," *Proc. of the 42nd Annual Meeting of The Institute of Navigation*, Seattle, WA, 1986, pp. 1-4.
- [2] Parkinson, B. W., and Axelrad, P., "Autonomous GPS Integrity Monitoring Using the Pseudorange Residual," *NAVIGATION*, Vol. 35, No. 2, 1988, pp. 225-274.
- [3] EU-US Cooperation on Satellite Navigation, WG C-ARAIM Technical Subgroup, "ARAIM Technical Subgroup Milestone 1 Report", 2012. available online : [http://ec.europa.eu/enterprise/newsroom/cf\\_getdocument.cfm?doc\\_id=7793](http://ec.europa.eu/enterprise/newsroom/cf_getdocument.cfm?doc_id=7793)
- [4] RTCA Special Committee 159, "Minimum Aviation System Performance Standards for the Local Area Augmentation System (LAAS)," *RTCA/DO-245*, 2004, Appendix D.
- [5] Blanch, J., Walter, T., and Enge, P., "Results on the Optimal Detection Statistic for Integrity Monitoring," *Proc. of ION ITM 2013*, San Diego, California, January 2013, pp. 262-273.
- [6] Joerger, M., Stevanovic, S., Chan, F.-C., Langel, S., and Pervan, B., "Integrity Risk and Continuity Risk for Fault Detection and Exclusion Using Solution Separation ARAIM," *Proc. of ION GNSS+ 2013*, Nashville, TN, September 2013, pp. 2702-2722.
- [7] Hwang, P. Y., Brown, R. G., "RAIM-FDE Revisited: A New Breakthrough In Availability Performance With NIOAIM (Novel Integrity-Optimized RAIM)," *NAVIGATION*, Vol. 53, No. 1, 2006, pp. 41-52.
- [8] Lee, Y. C., "Two New RAIM Methods Based on the Optimally Weighted Average Solution (OWAS) Concept," *NAVIGATION*, Vol. 54, No. 4, 2008, pp. 333-345.
- [9] Blanch, J., Walter, T., Enge, P., "Optimal Positioning for Advanced RAIM," *Proc. of ION ITM 2012*, Newport Beach, CA, January 2012, pp. 1624-1647.
- [10] Brenner, M., "Integrated GPS/Inertial Fault Detection Availability," *NAVIGATION*, Vol. 43, No. 2, 1996, pp. 111-130.
- [11] Blanch, J., Ene, A., Walter, T., and Enge, P., "An Optimized Multiple Hypothesis RAIM Algorithm for Vertical Guidance," *Proc. of ION GNSS 2007*, Fort Worth, TX, September 2007, pp. 2924-2933.
- [12] Potter, I. E., and Suman, M. C., "Threshold-less Redundancy Management With Arrays of Skewed Instruments," *AGARDOGRAPH - No 224*, 1977, pp 15-11 to 15-25.
- [13] Joerger, M., Chan, F.-C., and Pervan, B., "Solution Separation Versus Residual-Based RAIM," *NAVIGATION*, Vol. 61, 4.
- [14] Blanch, J., T. Walter, P. Enge, S. Wallner, F. A. Fernandez, R. Dellago, R. Ioannides, I. F. Hernandez, B. Belabbas, A. Spletter, M. Rippl, "Critical Elements for a Multi-Constellation Advanced RAIM," *NAVIGATION*, Vol. 60, No. 1, 2013, pp. 53-69.
- [15] DeCleene, B., "Defining Pseudorange Integrity – Overbounding," *Proc. of ION GPS 2000*, Salt Lake City, UT., 2000, pp. 1916-1924.
- [16] Drezner, Z., and Wesolowsky, G. O., "On the Computation of the Bivariate Normal Integral," *Journal of Statistical Computation and Simulation*, Vol. 35, 1989, pp. 101–107.
- [17] Luenberger, D. G., and Ye, Y., *Linear and Nonlinear Programming – Third Edition*, Springer Editor, 2008.
- [18] EU-US Cooperation on Satellite Navigation, WG C-ARAIM Technical Subgroup, "ARAIM Technical Subgroup Milestone 2-B Report", to be published end of 2014.